Article

Quarkonia Formation in a Holographic Gravity–Dilaton Background Describing QCD Thermodynamics

Rico Zöllner [1,*] and **Burkhard Kämpfer** [2]

[1] Helmholtz-Zentrum Dresden-Rossendorf, 01314 Dresden, Germany
[2] Institut für Theoretische Physik, TU Dresden, 01062 Dresden, Germany; kaempfer@hzdr.de
[*] Correspondence: rico@hierbeizoellners.de

Abstract: A holographic model of probe quarkonia is presented, where the dynamical gravity–dilaton background was adjusted to the thermodynamics of 2 + 1 flavor QCD with physical quark masses. The quarkonia action was modified to account for the systematic study of the heavy-quark mass dependence. We focused on the J/ψ and Υ spectral functions and related our model to heavy quarkonia formation as a special aspect of hadron phenomenology in heavy-ion collisions at LHC.

Keywords: AdS/CFT correspondence; QCD phenomenology; meson spectral functions

1. Introduction

Heavy-quark flavor degrees of freedom are currently receiving strong interest as valuable probes of hot and dense strong-interaction matter produced by the heavy-ion collisions at LHC energies. The information encoded, e.g., in quarkonia ($c\bar{c}$, $b\bar{b}$) observables, supplements penetrating electromagnetic probes and hard (jet) probes and the rich flow observables, thus complementing each other in characterizing the dynamics of quarks and gluons until the final hadronic states (cf., contributions in [1,2] for the state of the art). Since heavy quarks essentially emerge in early, hard processes, they witness the course of heavy-ion collision—either as individual entities or subjects of dissociating and regenerating bound states [3–5]. Accordingly, the heavy-quark physics addresses such issues as charm (c, $\bar{c}$) and bottom (b, $\bar{b}$) dynamics related to transport coefficients [6–10] in the rapidly evolving and highly anisotropic ambient quark–gluon medium [11,12] as well as $c\bar{c}$ and $b\bar{b}$ states as open quantum systems [13–16]. The rich body of experimental data from LHC, and also from RHIC , enabled a tremendous refinement of our understanding of heavy-quark dynamics. For a recent survey on quarkonium physics, we refer the interested reader to [17].

The yields of various hadron species, light nuclei and anti-nuclei—even such ones which are only very loosely bound [18]—emerging from heavy-ion collisions at LHC energies are described by the thermo-statistical hadronization model [19] with high accuracy. These yields span an interval of nine orders of magnitude. The final hadrons and nuclear clusters are described by two parameters: the freeze-out temperature $T_{fo} = 155$ MeV and a freeze-out volume depending on the system size or centrality of the collision. Due to the near-perfect matter–antimatter symmetry at top LHC energies, the baryo-chemical potential μ_B is exceedingly small, $\mu_B/T_{fo} \ll 1$. It is argued in [19] that the freeze-out of color-neutral objects only happens in the demarcation region of hadron matter to quark–gluon plasma, i.e., of confined vs. deconfined strong-interaction matter. In fact, the lattice QCD results report a pseudo-critical temperature of $T_c = (156 \pm 1.5)$ MeV [20]—a value agreeing with the disappearance of the chiral condensates and the maximum of some susceptibilities. The key is the adjustment of physical quark masses and the use of 2 + 1 flavors [21,22], in short, QCD_{2+1}(phys). Details of the (maybe accidental) coincidence of the deconfinement and chiral symmetry restoration are currently matters of debate [23], as is the formation of color-neutral objects out of the cooling quark–gluon plasma at T_c.

For instance, [24] advocates flavor-dependent freeze-out temperatures. Note that at T_c no phase transition happens, rather the thermodynamics is characterized by a cross-over accompanied by a pronounced dip in the sound velocity.

Among the tools for describing hadrons as composite strong-interaction systems is holography. Anchored in the famous AdS/CFT correspondence, holographic bottom-up approaches have facilitated a successful description of mass spectra, coupling strengths/decay constants, etc. of various hadron species. While the direct link to QCD by holographic QCD-dual or rigorous top–down formulations are still missing, one has to restrict the accessible observables to explore certain frameworks and scenarios. We consider here a minimal framework within the Einstein–dilaton model class, which merges (i) QCD_{2+1}(phys) thermodynamics, described by a dynamical holographic gravity–dilaton background, with (ii) holographic probe quarkonia. We envisaged a scenario which embodies the QCD thermodynamics of QCD_{2+1}(phys) and the emergence of hadron states at T_c at the same time. One motivation of our work was the exploration of a holographic model, which is in agreement with the above hadron phenomenology in heavy-ion collisions at LHC energies. Early holographic attempts [25–27] of hadrons at non-zero temperatures faced the problem of meson melting at temperatures significantly below the deconfinement temperature T_c. Several proposals have been made [28–31] to determine rescue avenues which accommodate hadrons at and below T_c. Otherwise, a series of holographic models of hadron melting without reference to QCD thermodynamics, e.g., [31–40], finds quarkonia states well above, at and below T_c in agreement with lattice QCD results [41–44]. It is therefore tempting to account for the proper QCD-related background.

We followed [45–48] and modelled the holographic background by a gravity–dilaton set-up, i.e., without adding further fundamental degrees of freedom (as done, e.g., in [49,50] and Refs. therein (The influence of the tachyon dual to the quark condensate can be neglected for heavy mesons.)) to the dilaton, which was originally solely related to the gluon degrees of freedom [51]. That is, the dilaton potential was adjusted to QCD_{2+1}(phys) lattice data. In the temperature region $T \approx \mathcal{O}(T_c)$, the impact of the charm and bottom degrees of freedom on the quark–gluon–hadron thermodynamics is minor [52]. Thus, we considered quarkonia as test particles. If the gravity–dilaton background is considered to be unique, it is known that there would be no confinement at zero temperature [48]. As we show, this problem can be efficiently solved by a less intricate generalization of the standard action of the soft-wall model [53] inspired by [54] which evince a principle to bring together QCD thermodynamics and the confinement of test particles at zero temperature. Our emphasis is on the formation of quarkonia in a cooling strong-interaction environment mimicking conditions in heavy-ion collisions at LHC. Thereby, the quarkonia properties are described by spectral functions.

Our paper is organized as follows. In Section 2, the dynamics of the probe quarkonia is formulated and the coupling to the thermodynamics-related background is explained (the recollection of the gravity–dilaton dynamics and the consideration of special features are relegated to Appendix A). Numerical solutions in the charm (J/ψ) and bottom (Y) sectors with respect to quarkonium's spectral functions and systematic formation are dealt with in Section 3. The tested two-parameter Schrödinger potential facilitates bottomonium formation through the rapid squeezing of the spectral function towards a narrow quasi-particle state in a small temperature interval around T_c. An analogous behavior is accomplished for charmonium by a three-parameter potential considered in Section 4. The squeezing of the charmonium spectral function extends over a somewhat longer temperature interval and requires a particular parameter setting. We summarize in Section 5.

2. Quarkonia as Probe Vector Mesons

The action of quarkonia as probe vector mesons in string frame is:

$$S_m^V = \frac{1}{k_V} \int \mathrm{d}^4x \, \mathrm{d}z \sqrt{g_5} e^{-\phi} \, G_m(\phi) \, F^2,$$

(1)

where the function $G_m(\phi)$ carries the flavor (or heavy-quark mass, labeled by m) dependence and F^2 is the field strength tensor squared of a $U(1)$ gauge field $\mathcal{A}$ in 5D asymptotic anti-de Sitter (AdS) space time, with or without a black hole (BH), with the bulk coordinate z and metric fundamental determinant g_5; ϕ is the scalar dilatonic field with a zero mass dimension. The gauge field $\mathcal{A}$ in the bulk was sourced by a current operator of the structure $\bar{Q}\gamma_\mu Q$ at the boundary, where Q stands for the heavy quark field operator. The structure of (1) is that of a field-dependent gauge kinetic term, familiar, e.g., from realizations of a localization mechanism in brane world scenarios [55–57].

The action (1) with $G_m = 1$, originally put forward in the soft-wall (SW) model for light-quark mesons [53], is also used for describing heavy-quark vector mesons [32–34], e.g., charmonium [35,36] or bottomonium [58]. As emphasized, e.g., in [35], the holographic background encoded in g_5 and ϕ must be chosen differently to imprint the different mass scales, since (1) with $G_m = 1$ as such would be flavor blind. Clearly, the combination $\exp\{-\phi\}G_m(\phi)$ in (1) with flavor-dependent function $G_m(\phi)$ is nothing but effectively introducing a flavor-dependent dilaton profile $\phi_m = \phi - \log G_m$, while keeping the thermodynamics-steered hadron-universal dilaton ϕ. In fact, many authors use the form $S_m^V = \frac{1}{k_V} \int \mathrm{d}^4x \, \mathrm{d}z \sqrt{g_5} e^{-\phi_m} F^2$ to study the vector meson melting by employing different parameterizations of ϕ_m to account for different flavor sectors. Here, we emphasize the use of a unique gravity–dilaton background for all flavors and include the quark mass (or flavor) dependence solely in G_m.

Our procedure to determine G_m was based on the import of information from the hadron sector at $T = 0$. The action (1) leads via the gauges $\mathcal{A}_z = 0$ and $\partial^\mu \mathcal{A}_\mu = 0$ and the ansatz $\mathcal{A}_\mu = \epsilon_\mu \, \varphi(z) \exp\{ip_\nu x^\nu\}$ with $\mu, \nu = 0, \cdots, 3$, which uniformly separates the z dependence of the gauge field by the bulk-to-boundary propagator φ for all components of $\mathcal{A}$, and the constant polarization vector ϵ_μ to the equation of motion:

$$\varphi'' + \left[\frac{1}{2}A' + (\partial_\phi \log G_m - 1)\phi' + (\log f)'\right]\varphi' + \frac{p^\mu p_\mu}{f^2}\varphi = 0, \tag{2}$$

where $A(z, z_H)$ is the warp factor and $f(z, z_H)$ denotes the blackening function in the AdS + BH metric with a horizon at z_H:

$$\mathrm{d}s^2 = \exp\{A(z, z_H)\}\left[f(z, z_H)\,\mathrm{d}t^2 - \mathrm{d}\vec{x}^2 - \frac{\mathrm{d}z^2}{f(z, z_H)}\right], \tag{3}$$

and a prime denotes the derivative with respect to the bulk coordinate z. Both $A(z, z_H)$ and $f(z, z_H)$ are solutions of Einstein's equation with a dilatonic potential adjusted to QCD thermodynamics with physical quark masses in the temperature range 100 MeV $< T < 400$ MeV (cf., Appendix A in [59] and Appendix A for more details); $\phi(z, z_H)$ is also dynamically determined and is consistent with the metric coefficients via field equations.

By the transformation $\psi(\xi) = \varphi(z(\xi)) \exp\{\frac{1}{2}\int_0^\xi \mathrm{d}z \, \mathcal{S}_T(\xi)\}$ one gets the form of a one-dimensional Schrödinger equation with the tortoise coordinate ξ:

$$\left[\partial_\xi^2 - (U_T(z(\xi)) - m_n^2)\right]\psi_n(\xi) = 0, \quad n = 0, 1, 2, \cdots, \tag{4}$$

where one has to employ $z(\xi)$ from solving $\partial_\xi = (1/f)\partial_z$. The Schrödinger equivalent potential is:

$$U_T \equiv \left(\frac{1}{2}\mathcal{S}_T' + \frac{1}{4}\mathcal{S}_T^2\right)f^2 + \frac{1}{2}\mathcal{S}_T f f' \tag{5}$$

as a function of $\xi(z)$ with:

$$\mathcal{S}_T \equiv \frac{1}{2}A' - \phi' + \partial_z \log G_m(\phi(z)). \tag{6}$$

At $T = 0$ (label "0"), $f = 1$ and $\xi \to z$ and $U_T \to U_0$ with:

$$U_0(z) \equiv \frac{1}{2}\mathcal{S}_0' + \frac{1}{4}\mathcal{S}_0^2, \tag{7}$$

$$\mathcal{S}_0 \equiv \frac{1}{2}A_0'(z) - \phi_0'(z) + \partial_z \log G_m(\phi_0(z)), \tag{8}$$

and (4) becomes:

$$\left[\partial_z^2 + (U_0(z) - m_n^2)\right]\psi_n = 0 \tag{9}$$

with normalizable solutions ψ_n and discrete states with masses squared $m_n^2 = p^\mu p_\mu$, $n = 0, 1, 2, \cdots$ for quarkonia at rest. That is, at $T = 0$, one has to deal with a suitable Schrödinger equivalent potential $U_0(z)$ to generate the desired spectrum m_n. In such a way, the needed hadron physics information at $T = 0$ is imported by parameterizing U_0 in a suitable manner (see Sections 3 and 4).

The next step is solving (7) to obtain $\mathcal{S}_0(z)$ and with (8), then $G_m(\phi)$ with $G_m(0) = 1$. This procedure requires the knowledge of the warp factor $A_0(z)$ and the dilaton profile $\phi_0(z)$, which are determined by Equations (A2)–(A4) in Appendix A. The governing dilaton potential $V(\phi)$ in turn is found by an adjustment to lattice QCD data. On the one hand, at $T < 100$ MeV, there are nearly no lattice QCD data of the needed thermodynamic quantities, such as sound velocity and entropy etc., at our disposal. On the other hand, at $T > 100$ MeV the rich body of lattice QCD data has, despite the great progress made, still non-negligible error bars. We therefore must assume that the ansatz (A5) delivers an adequate representation of the QCD input (see Figure 5-left in [59] for the sound velocity squared). Leaving a dedicated investigation of the potential impact of variations of $V(\phi)$ under constraints of lattice QCD thermodynamics data for follow-up work, we then used the so determined $G_m(\phi) = G_m(z(\phi_0))$ as universal (i.e., temperature-independent) function.

The equation of motion (2) of φ can also be employed to compute quarkonia spectral functions, cf., [25,33–35,60]. For $\omega^2 = p^\mu p_\mu > 0$ fixed, the asymptotic boundary behavior facilitates two linearly independent solutions by considering the leading order terms on both sides of the interval $[0, z_H]$. (i) For $z \to 0$, one has, due to the AdS asymptotics at the boundary, the general solution is:

$$\varphi(z \to 0) \to A(\omega)\varphi_1 + B(\omega)\varphi_2 \tag{10}$$

with two ω-dependent complex constants A and B, and $\varphi_1(z \to 0) \to 1$ and $\varphi_2(z \to 0) \to (z/z_H)^2$; (ii) near the horizon, $z \to z_H$, the asymptotic behavior of solutions of (2) is steered by the poles of $1/f$ and $1/f^2$. The two linearly independent solutions are $\varphi_\pm(z \to z_H) \to (1 - \frac{z}{z_H})^{\pm i\omega/|f'(z_H)|}$, where $\varphi_\pm$ represent out-going and in-falling solutions, respectively. The obvious and commonly used side conditions for the bulk-to-boundary propagator are $\varphi(0) = 1$, which means $A(\omega) = 1$, and $\varphi(z \to z_H) = \varphi_-(z \to z_H)$ (purely in-falling solution at the black hole horizon).

Then, the corresponding retarded Green function $\mathcal{G}^R$ of the dual current operator $\bar{Q}\gamma_\mu Q$, defined within the framework of the holographic dictionary via a generating functional by $\mathcal{G}^R = \frac{\delta^2}{\delta \mathcal{A}^{0\mu}(-\omega)\delta \mathcal{A}_\mu^0(\omega)}\langle\exp\{i\int d^4x\, \mathcal{A}_\nu^0 \bar{Q}\gamma^\nu Q\}\rangle$, is given by (cf., [61])

$$\mathcal{G}^R(\omega) = \frac{\delta^2 S_m^{V,\text{on-shell}}}{\delta \mathcal{A}^{0\mu}(-\omega)\,\delta \mathcal{A}_\mu^0(\omega)} = k \lim_{z \to 0}\frac{1}{z}\varphi^*(z)\varphi'(z) = \frac{2k}{z_H^2}B(\omega) \tag{11}$$

with $k = \frac{N_c}{24\pi^2}$ and $\mathcal{A}_\mu^0 \equiv \epsilon_\mu \exp\{ip_\nu x^\nu\}$ for $\mu \in \{1, 2, 3\}$. The quantity $S_m^{V,\text{on-shell}}$ denotes here the action (1) with the solution φ from (2). Finally, the spectral function ρ follows from $\rho(\omega) = \text{Im}\,\mathcal{G}^R(\omega) = \frac{2k}{z_H^2}\text{Im}\,B(\omega)$.

3. Two-Parameter Potential—Bottomonium Formation

Our setting does not explicitly refer to a certain quark mass m. Instead, an ansatz $U_0(z; \vec{p})$ with a parameter n-tuple $\{\vec{p}\}$ was used such to catch a certain quarkonium mass spectrum. Therefore, m is to be considered as a cumulative label highlighting the dependence of G_m on a parameter set $\{\vec{p}\}$ which originally enters U_0 and which is to be adjusted to the charmonium and bottomonium masses observed in nature.

As a transparent model, we select the two-parameter potential [33,35]:

$$U_0(z) = \frac{3}{4}\left(\frac{1}{z}\right)^2 + a^2 z^2 / L^4 + 4b/L^2 \tag{12}$$

which is known to deliver via (9) the normalizable functions ψ_n with discrete eigenvalues:

$$L^2 m_n^2 = 4(a + b + n\,a), \quad n = 0, 1, 2, \cdots. \tag{13}$$

The potential (12) is a slight modification of the SW model [53]. We choose these parameters as follows. The mass m_0 determines the ground state (g.s.) "trajectory" in the a-b plane, $b = \frac{1}{4}L^2 m_0^2 - a$, and m_1 determines the first excitation (1st) "trajectory" by $b = \frac{1}{4}L^2 m_1^2 - 2a$. Using the PDG values of J/ψ, ψ' and $\Upsilon(1S, 2S)$ adjusts the "trajectories" as solid and dashed lines in Figure 1, where we employ the scale setting with $L^{-1} = 1.99$ GeV, which is related to the QCD thermodynamics sector (see Appendix A in [59]). Allowing for a 10% variation of m_1, one arrives at the colored bands in Figure 1. By such a parameter choice, one places emphasis on the quarkonia g.s. masses as representatives of the heavy quark masses and less emphasis on the level spacing of excitations and ignores other possible constraints.
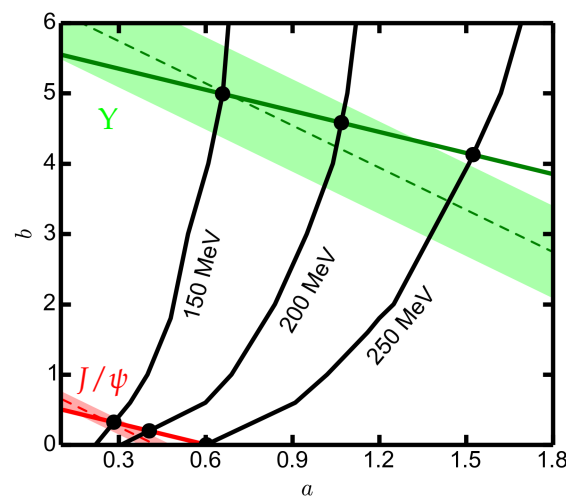

Figure 1. Constant ground state masses (fat solid lines) and the respective first excitations (dashed lines; a $\pm 5\%$ corridor is depicted by colored bands) at $T = 0$ over the dimensionless a–b plane of the potential (12). Color code: green—Υ; red—J/ψ. The bullets mark selected parameters for the spectral functions exhibited in Figure 2. The black curves exhibit the loci at which the peaks of the spectral functions completely disappear, i.e., they represent the contours of melting temperatures $T_{melt}^{g.s.}(a, b) = 150, 200,$ and 250 MeV. That is, for a given point (a, b) in the parameter space, the spectral function in the energy range of the ground state displays a peak only for $T < T_{melt}^{g.s.}$.

As we shall demonstrate below, the ansatz (12) has several drawbacks, and therefore, is to be considered as an illustrative example. For instance, the sequence of radial Υ excitations in nature does not form a strictly linear Regge trajectory [62]. This prevents an unambiguous mapping of $m_{0,1} \mapsto (a, b)$. While the radial excitations of J/ψ follow quite accurately a linear Regge trajectory in nature [62], the request for accommodating further

J/ψ properties in U_0 also calls for modifying (12), cf., [35,60]. Despite the mentioned deficits, the appeal of (12) and (13) is nevertheless the simply invertible relation $m_n^2(a, b)$ yielding $a(m_{0,1})$ and $b(m_{0,1})$. Since we are going to study the systematic, we retain the primary parameters a and b in what follows. Instead of discussing the results at isolated points in parameter space referring to J/ψ and Υ ground states m_0 and first excited states m_1, we consider the systematic over the a-b plane.

The black curves in Figure 1 exhibit the contours $T_{melt}^{g.s.}(a, b) = 150$, 200, and 250 MeV. The melting temperature $T_{melt}^{g.s.}$ is determined by the disappearance of the peak of the g.s. spectral function upon the temperature increase. One observes a strong parameter dependence as well, which determines the spectral functions, as can be seen in Figure 2. Changing the parameters (a, b) deforms the potential (12) in a characteristic manner [59], e.g., going on a g.s. trajectory to the right squeezes the excited states to higher energies, as can be identified in Figure 1, in particular for the Υ. Such changes immediately affect the spectral functions.
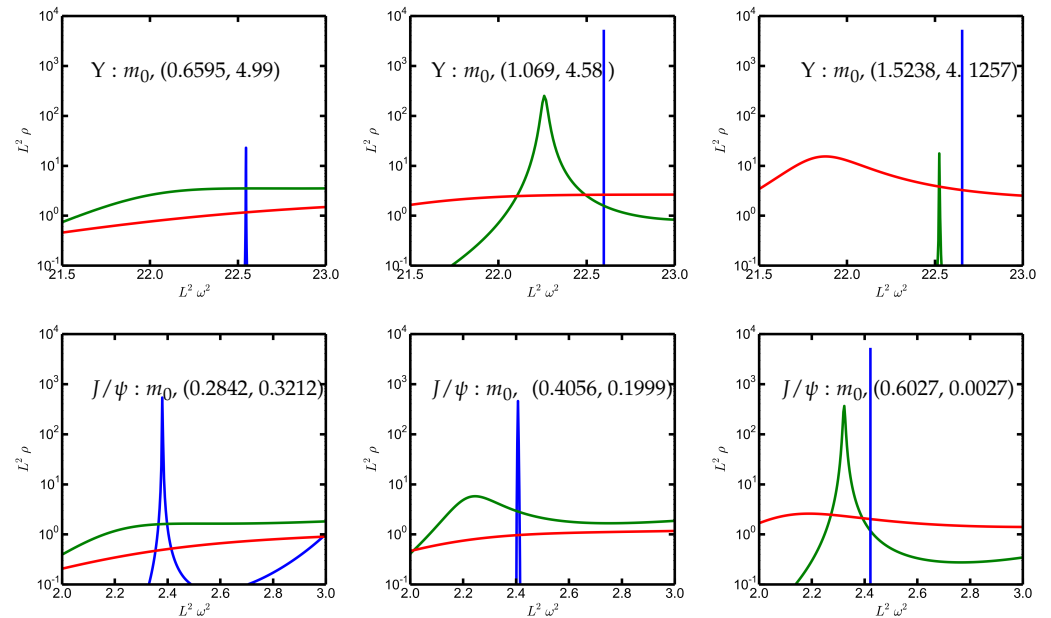

Figure 2. Spectral functions $L^2\rho(\omega, T)$ of Υ (**top row**) and J/ψ (**bottom row**) in the ground state (g.s.) energy region at $T = 100$ (blue), 150 (green), and 200 MeV (red). For parameters (a, b) on the g.s. trajectories, i.e., for PDG values of m_0. The values of (a, b) are given in the legends; these positions are marked in Figure 1 by bullets.

In Figure 1, it looks like an accidental coincidence that, at the crossing points of the g.s. and first excitation trajectories of J/ψ and Υ, the melting temperature is 150 MeV. In other words, in a cooling system, the formation of the quarkonium ground state seems to start when passing the temperature of 150 MeV. This is consistent with the claim in [19] which advocates the formation of hadron states at $T \approx 155$ MeV $\approx T_c$. Consistency does not necessarily mean perfect agreement. The criteria for "melting" or "onset of formation" are not very precise. For instance, [60] uses the relative high of the spectral function's peak over the smooth background as a threshold value to define "melting". The transition to a quasi-particle with sharp spectral function does not happen instantaneously but within some temperature span, as can be seen in the top panels in Figures 3 and 4. Considering the dynamics of the cooling system as a sequence of equilibrium states, the spectral-function contour-plots in Figures 3 and 4 are suggestive: upon cooling, the strength of a hadron state is consecutively concentrated to a narrow energy range, eventually forming the quasi-particle. Displaying a spectral function at a few selected temperatures, as in Figure 2, and

bottom panels of Figures 3 and 4 as well, only insufficiently illustrates such a feature but is useful for a more quantitative account.

The inspection of the top panels of Figures 3 and 4 unravels that the temperature difference from $T_{melt}^{g.s.}$ until the formation of a sharp quasi-particle state is quite large. Sharp quasi-particles can be identified by the squeezed contour lines which eventually nearly coincide with the peak position of the spectral functions depicted by the red dashed curves in the top panels of Figures 3 and 4. Keeping the quarkonia ground state masses m_0 and artificially allowing for a somewhat larger value of the first excited state m_1 moves the quarkonia formation temperatures to larger values, in particular for Y, as can be seen in the right panels in Figure 3. In such a way, the quasi-particle formation temperature $T_{form}^{Y(1S)} \approx T_c$ copes with the claim in [19] of hadron formation at T_c. The J/ψ, in contrast, would be formed at $T_{form}^{J/\psi} < T_c$ (see Figure 4) in conflict with the advertisement of [19]. Section 4 provides a potential ansatz $U_0(z; \vec{p})$ which accomplishes $T_{form}^{J/\psi} \approx T_c$.
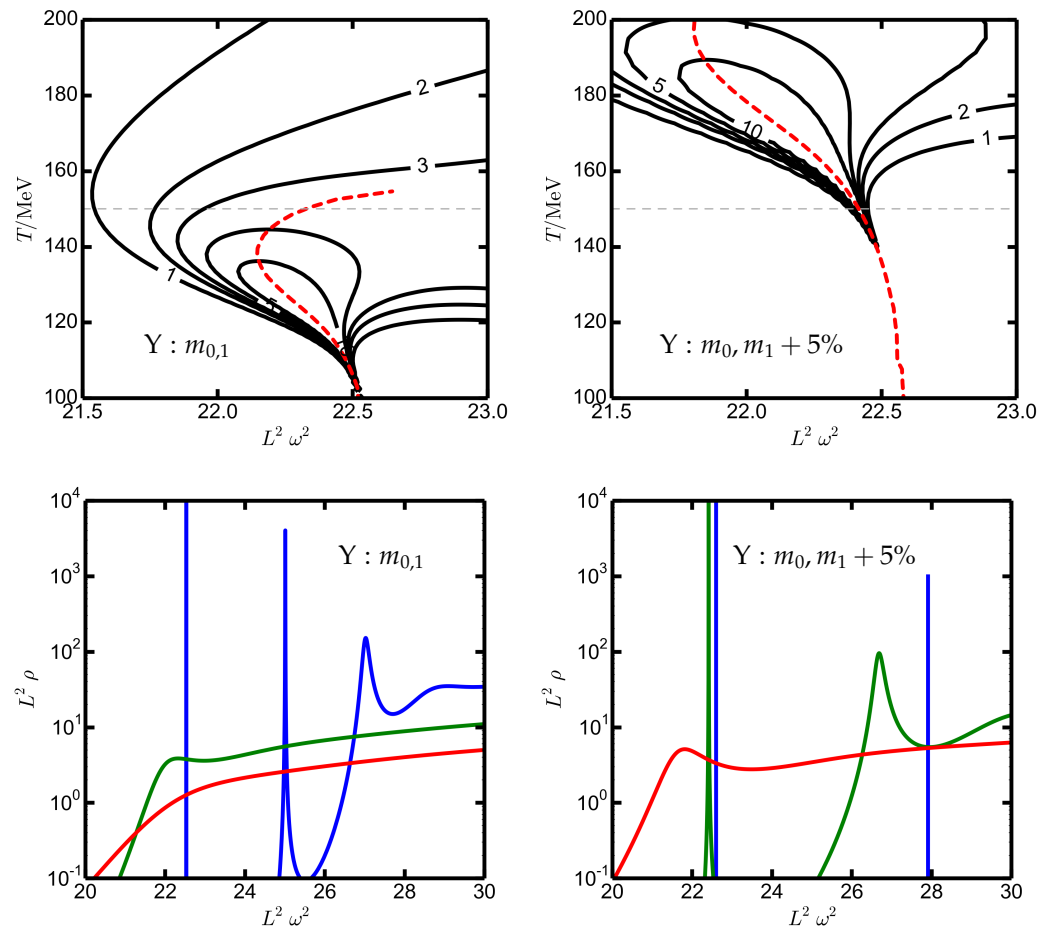

Figure 3. Bottomonium formation. **Top row**: contour plots of the spectral functions $L^2\rho(\omega, T)$ (the red dashed curves depict the peak position of the respective spectral function; they terminate at T_{melt}; dashed horizontal lines indicate $T = 150$ MeV), **bottom row**: spectral functions $L^2\rho(\omega, T)$ at several temperatures ($T = 100$ (blue), 150 (green), and 200 MeV (red), **left column**: for potential parameters $(a, b) = (0.6924, 4.9571)$, i.e., at such values where the $m_{0,1}(a, b)$ trajectories cross; **right column**: $(a, b) = (1.3266, 4.3229)$, i.e., at crossing points of the m_0 trajectory with the upper limit of the 10% corridor of the respective first excitation ($T_{melt}^{g.s.} = 234$ MeV).
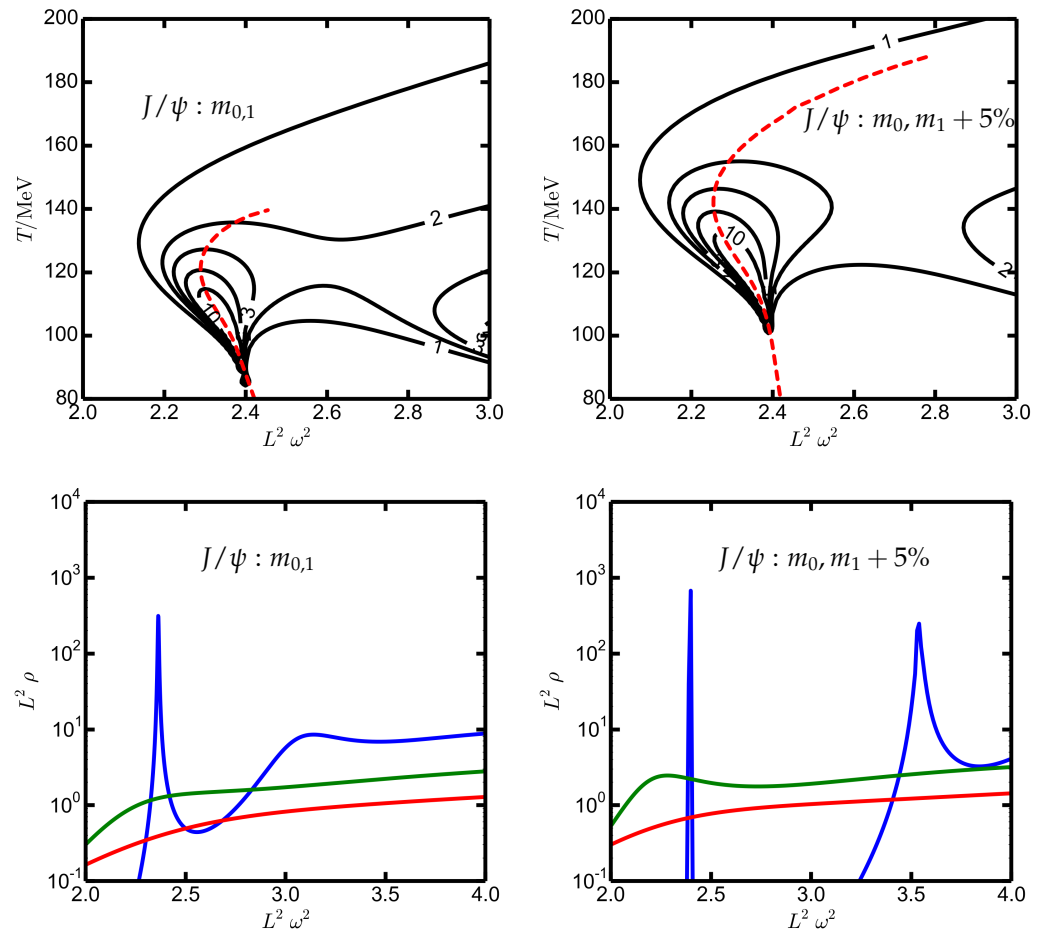
Figure 4. Charmonium formation. **Top row**: contour plots of the spectral functions $L^2\rho(\omega, T)$, **bottom row**: spectral functions $L^2\rho(\omega, T)$ in the energy region of g.s. and first excitation at several temperatures ($T = 100$ (blue), 150 (green), and 200 MeV (red)), **left column**: $(a, b) = (0.2522, 0.3533)$ i.e., at such values where the $m_{0,1}(a, b)$ trajectories cross; **right column**: $(a, b) = (0.338, 0.2675)$, i.e., at crossing points of the m_0 trajectory with the upper limit of the 10% corridor of the respective first excitation.

To understand why the J/ψ (Υ) reacts so sluggishly (violently) on a modification of m_1 while keeping m_0 fixed, we mention that the parameter a in (12) changes by 33% (92%, i.e., a factor of nearly two) upon a 5% increase in m_1, (due to the non-linearity of the $J^{PC} = 1^{--}$ bottomonium Regge trajectory, the energy of $m_1 + 5\%$ is between the $3^3S_1/\Upsilon(3S)$ and $4^3S_1/\Upsilon(4S)$ states. For charmonium, in contrast, $m_1 + 5\%$ is well below the $3^3S_1/\psi(4040)$ state, cf., [62].) which is to been seen in connection with the curvature $8a^2$ of U_0 at the minimum $z_{min}/L = \left(3/(4a^2)\right)^{1/4}$. The more the potential U_0 is squeezed by parameter variation, e.g., by larger values of $\hat{a}$, the less sensitive the temperature of is U_T, as can be seen in Figure 2 in [59] and Figure 6 below. At the origin of these differences is the ratio of m_1^2/m_0^2 which is 1.42 for J/ψ and 1.12 for Υ, respectively. It enters the scaled potential (12) $U_0(\hat{z} \equiv m_0 z, \zeta \equiv m_1^2/m_0^2 - 1)/m_0^2 = \frac{3}{4}\hat{z}^{-2} + \frac{1}{16}\zeta^2\hat{z}^2 - \zeta + 1$ solely as a parameter.

A second issue refers to the formation of excited states. It seems to be a generic feature of the holographic model class considered here that higher excited states would form at lower temperatures than the respective g.s.—in particular $T_{form}^{g.s.} > T_{form}^{1st} > T_{form}^{2nd} \cdots$, as can be seen in the bottom panels in Figures 3 and 4. The conjecture of [19], in contrast, advocates $T_{form}^{g.s.} \approx T_{form}^{1st}$. This feature is to be seen in relation to the considered ansatz of $U_0(z; a, b)$ with the IR behavior $\propto z^2$: a much steeper increase in U_0 at larger values of z would concentrate the melting temperatures in a narrow corridor.

In addition to the ansat, (12) facilitates a sequential quarkonium formation upon decreasing temperature, $T_{form}^{g.s.} > T_{form}^{1st} > T_{form}^{2nd}$ etc., which potentially allows for some flavor dependence, e.g., $T_{form}^{Y(1S)} > T_{form}^{J/\psi}$. The thermal mass shifts have a non-trivial temperature dependence as evidenced in Figure 5. Such thermal mass shifts are employed in [9] to pin down the heavy-quark (HQ) transport coefficient γ which can be considered as the dispersive counterpart of the HQ momentum diffusion coefficient $\kappa = 2T^3/(DT)$, where D stands for the HQ spatial diffusion coefficient. In [17], the author seemingly stresses a tension within previous holographic results [36], where positive mass shifts are reported, in contrast to negative shifts, e.g., in [34]. Our set-up qualitatively resolves this issue since, depending on the considered temperature, the thermal mass shift can be negative or positive, see Figure 5. One should note, however, that our thermal mass shifts of J/ψ and Y are larger than the lattice QCD-based values quoted in [9,44].
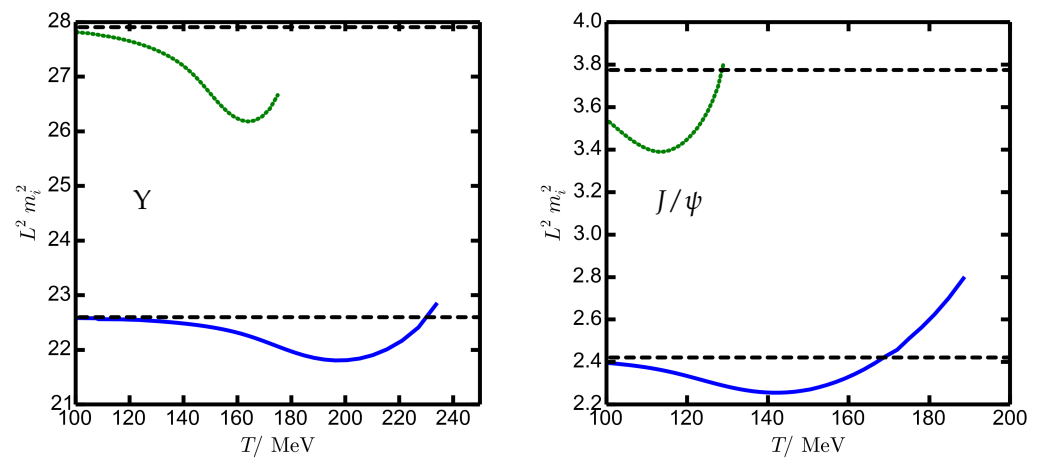

Figure 5. Positions of the peaks of the spectral functions of Y (**left panel**) and J/ψ (**right panel**) as a function of temperature. The right end points of the solid curves define T_{melt} fore the g.s. (lower blue solid curves) and first excitation (upper green dotted curves). The dashed lines depict the masses squared at $T = 0$. The difference of the solid or dotted curves to the dashed lines is termed "thermal mass shift" squared. For $(a, b) = (1.3266, 4.3229)|_Y$ and $(0.338, 0.2675)|_{J/\psi}$, as in the right columns of Figures 3 and 4.

Finally, let us remind that the two-parameter ansatz (12) is appealing since it allows for analytic solutions with respect to the excitation spectrum and an easy overview of the parameter dependencies. However, the authors of [35,60] already promoted (12) a "shift and dip potential" to catch more properties of the J/ψ states rather than only masses.

4. Three-Parameter Potential with Dip—Charmonium Formation

The two-parameter potential $U_0(z; a, b)$ from (12) with the realistic values of $a(m_{0,1})$ and $b(m_{0,1})$ facilitate J/ψ formation at too low temperatures. This failure can be repaired by turning to more appropriate parameterizations. For instance, [35,60] proposed a four-parameter "dip and shift potential" which allows for J/ψ melting temperatures significantly above T_c, as does the construction in [31–34,36] deploying three parameters. The essence is a dip in $U_0(z; \vec{p})$ which holds together the spectral strength despite large temperatures. Here, we consider such an option. The difference to previous work is the use of the dynamical background related to QCD, as described in Appendix A.

The construction of a particular three-parameter potential $U_0(z; M, k, \Gamma)$ is as follows. Use $A_0(z) = -2\log z/L$ and $\phi_0(z; M, k, \Gamma) = k^2 z^2 + Mz + \tanh x$ [58] with $x \equiv 1/Mz - k/\sqrt{\Gamma}$. Due to $U_0 = \frac{1}{2}(\frac{1}{2}A_0' - \phi_0')' + \frac{1}{4}(\frac{1}{2}A_0' - \phi_0')^2$ (see (7) and (8)) the potential is given by

$$
\begin{aligned}
U_0(z; M, k, \Gamma) &= \frac{3}{2z^2} + \frac{1}{4}M^2 + k^4 z^2 + \frac{M}{2z} + k^2 Mz \\
&\quad - \left(\frac{3}{2Mz^3} + \frac{1}{2z^2} + \frac{k^2}{Mz} \right) \frac{1}{\cosh^2 x} \\
&\quad + \frac{1}{4M^2 z^4} [4\sinh x \, \cosh x + 1] \frac{1}{\cosh^4 x}.
\end{aligned}
\tag{14}
$$

The first three terms in the top line suggest a correspondence $M \hat{=} 4\sqrt{b}/L$ and $k \hat{=} \sqrt{a}/L$ by a comparison with (12), while the next two terms cause some modification of (12) at intermediate values of z. The second line of (14) is essentially responsible for the dip—somewhat modified by terms in the third line. The dip position is determined to a large extent by the $1/\cosh^2$ term which peaks at $z = \sqrt{\Gamma}/(kM)$; the sinh term in the third line shifts the dip tip to smaller values of z. The UV and IR asymptotics are the same as for the potential (12). The dip position and the dip depth are interrelated, in contrast to the construction in [35,60].

The potential (14) might exhibit some non-trivial local structures as a function of z for particular parameters. In [58], the author advocates the optimum parameters $M = 2.2$ GeV (representing a mass scale of non-hadronic decays); $k = 1.2$ GeV (representing the quark mass); and $\sqrt{\Gamma} = 0.55$ GeV (representing the $Q\bar{Q}$ string tension) to yield the J/ψ (ψ') mass of 2.943 (3.959) GeV and the decay constant of 399 (255) MeV (see Table I in [58], the entries displaying "Holographic Results for Charmonium"). Note the resulting overestimated level spacing quantified by $m_1^2/m_0^2 = 1.81$, in contrast to the PDG value of 1.42, when deploying these parameters.

Completely analog to the two-parameter potential (12), increasing the parameter k at $M \approx const$, the potential (14) is squeezed and becomes deeper. Analogously, decreasing the parameter $\sqrt{\Gamma}$ at constant values of k and M lets drop the absolute minimum of U_0. One may select such parameter pairs of (k, M) at a constant $\sqrt{\Gamma}$ to keep the g.s. mass m_0 constant, see the horizontal dashed line the in left panel of Figure 6. Due to the squeezing of the potential, the interior (left) part was less influenced when imposing a horizon at z_H, where $U_T(z = z_H) = 0$ is facilitated according to (5). As a result, the more the potential is squeezed, the smaller the values of z_H are which are allowed to hold the J/ψ prior to melting. This is the very reason which forces us to enlarge the parameter k (or a in (12)) to achieve quarkonium formation at sufficiently high temperatures in agreement with the perspective put forward in [19]. The dip in the potential (14) is useful in that respect since enlarging the parameter a in the flat potential (12) influenced the quarkonium formation in a less effective manner for J/ψ. Let us emphasize that we put more weight on the g.s. mass m_0 (see the fat solid curve in the right panel of Figure 6) as the representative of the quark mass, while we relaxed the constraint on the excited state m_1 to be in a realistic range (see the dashed curve and colored band in the right panel of Figure 6), thus following the rationale in [35].

Having U_0 at our disposal, we proceed as in Section 3. The contour plots of the J/ψ spectral function are exhibited in the top panels of Figure 7. One observes again the tendency of charmonium formation as a narrow corridor of contour lines at too low temperatures for parameters delivering exactly the PDG values of $m_{0,1}$, as can be seen in the left top panel. This is quantified by the spectral functions shown in the left bottom panel of Figure 7 which display only a broad peak at $T = 150$ MeV. Modifying the parameters as such to catch m_0 and $m_1 + 5\%$ DPG values significantly improves the approach to charmonium formation near T_c, as can be seen in the right panels of Figure 7, despite the yet imperfect squeezing of the contour lines in the right top panel. Nevertheless, the spectral function becomes well peaked at $T = 150$ MeV, as can be seen in the right bottom panel of Figure 7.
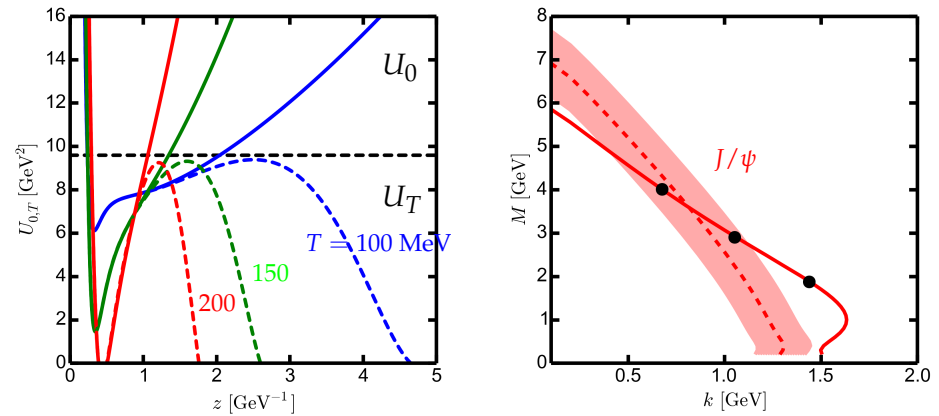
Figure 6. Left panel: the potential U_0 from (14) (upper fat solid curves) and the resulting U_T from (5)–(8) (lower dashed curves) as a function of z for $\sqrt{\Gamma} = 1.5$ GeV and values $(k, M) = (0.676, 4.007)$ (blue), $(1.053, 2.90)$ (green), and $(1.44, 1.87)$ (red). The dashed horizontal line depicts the J/ψ g.s. mass squared m_0^2 from U_0 which is the same for all three parameter selections. **Right panel**: the $m_{0,1}$ trajectories with PDG values in the k-M plane at $\sqrt{\Gamma} = 1.5$ GeV. The $m_1 \pm 5\%$ corridor is depicted as a colored band. The three parameter pairs (k, M) of the left panel are shown by bullets.
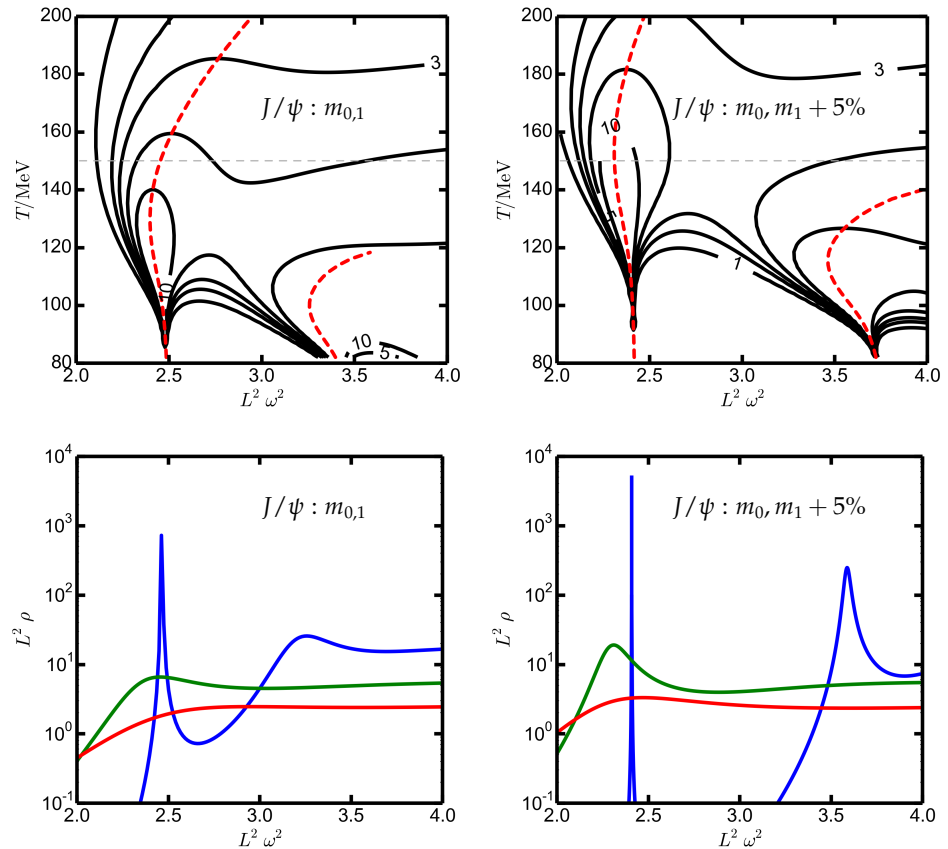

Figure 7. Charmonium formation in the three-parameter potential (14). **Top row**: contour plots of the spectral functions (the red dashed red curves depict the peak positions of the spectral functions); **bottom row**: spectral functions for a few selected values of the temperature, $T = 100$ (blue), 150 (green), and 200 MeV (red); **left column**: $(\sqrt{\Gamma}, k, M) = (1.0, 0.825, 3.656)$ GeV (yielding PDG values of $m_{0,1}$, $T_{melt}^{\text{g.s.}} = 228$ MeV); **right column**: $(\sqrt{\Gamma}, k, M) = (1.0, 0.9818, 3.1398)$ GeV (yielding m_0 and $m_1 + 5\%$, $T_{melt}^{\text{g.s.}} = 361$ MeV).

Finally, we exhibit in Figure 8 the contour plot of the charmonium spectral function (left panel) and the spectral function at selected temperatures (right panel) for the parameter set $(\sqrt{\Gamma}, k, M) = (0.55, 1.2, 2.2)$ GeV favored in [58]. These parameters, albeit with noticeable deviations to the PDG values of $m_{0,1}$, realize the charmonium formation as a transition from the spectral function to a narrow, quasi-particle state at temperatures slightly below T_c. While the squeezing of the contour lines near T_c in the left panel of Figure 8 is apparently not so pronounced as in the case of bottomonium (see right top panel in Figure 3), the spectral function displays a sharp peak at T_c, see right panel of Figure 8. Insofar, it is justified to speak on charmonium formation at T_c for the given parameter set. We emphasize the QCD-related background employed here, in contrast to the schematic background in [58].
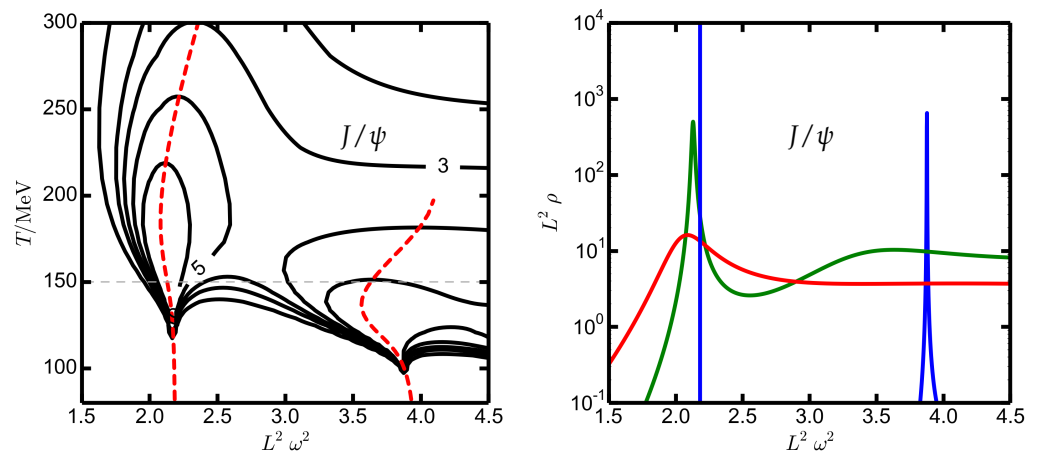

Figure 8. Charmonium formation in the potential (14) for the parameter set $(\sqrt{\Gamma}, k, M) = (0.55, 1.2, 2.2)$ GeV favored in [58], here combined with the QCD-related background. **Left panel**: contour plot of the charmonium spectral function $L^2\rho$. The dashed red curves are for the first two peak positions ($T_{melt}^{\text{g.s.}} = 464$ MeV). The dashed horizontal line indicates $T = 150$ MeV; **Right panel**: spectral functions $L^2\rho$ at temperatures of 100 (blue), 150 (green), and 200 (red) MeV.

To complete the systematic related to charmonium, we exhibit in Figure 9 the quantity $-\log G_m$ as a function of ϕ. Note the huge variation of $G_m(\phi)$. In general, $G_m(\phi)$ sensitively depends on the parameters in U_0 and is tightly related to the background.

An analog study of the Y formation is hampered by some uncomfortable structures of $U_0(z; M, k, \Gamma)$. References [31,32,36] advocate parameters which avoid such obstacles, however, these result in a value of $m_0^2(Y(1S))$ being only one half of the PDG value. We therefore did not perform an analysis of the potential ansatz (14) in the QCD-related background since the two-parameter potential (12) was already shown to successfully accomplish bottomonium formation at T_c.
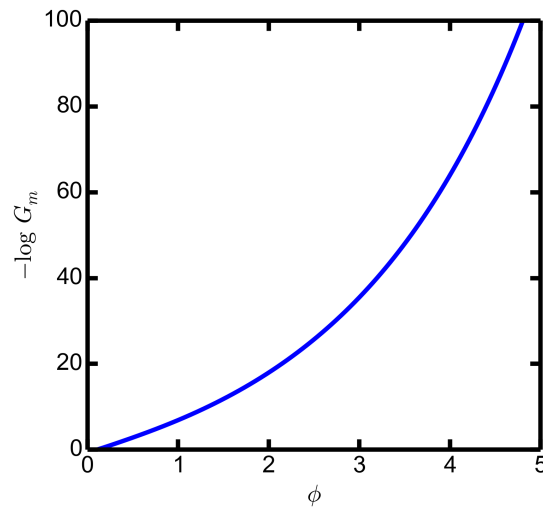
Figure 9. The quantity $-\log G_m(\phi)$ calculated from Equations (7) and (8) with A'_0, ϕ'_0 deduced from the thermodynamics in Appendix A and the potential (14) with $(\sqrt{\Gamma}, k, M) = (1.0, 0.825, 3.656)$ GeV yielding PDG values of charmonium masses $m_{0,1}$. $G_m(\phi)$ is supposed to be independent of temperature.

5. Summary

In summary, we introduced a modification of the holographic vector meson action for quarkonia such to join (i) the QCD_{2+1}(phys) thermodynamics, dynamically and consistently described by a dilaton and the metric coefficients in AdS + BH, with (ii) realistic quarkonia masses at zero temperature. Both pillars, thermodynamics and quarkonium mass spectra, are anchored in QCD as a common footing. The formal holographic construction was based on an effective dilaton $\phi_m = \phi - \log G_m$, where ϕ is solely tight to the light-quark–gluon thermodynamics background, while the flavor-dependent quantity G_m is determined by a combination of ϕ and the adopted Schrödinger equivalent potential U_0 at zero temperature. U_0 encodes the flavor (or quark mass) dependence and can be chosen with much sophistication to accommodate many quarkonia properties. We explore here the systematic of a two-parameter model to demonstrate the features of our scheme, where the thermodynamic background at $T > 0$ and meson spectra at $T = 0$ serve as a QCD-based input to analyze the quarkonia formation at $T > 0$. We tested a scenario where quarkonium formation was considered as an adiabatic process, i.e., a sequence of equilibrium states, and characterized by the shrinking of the respective spectral functions towards narrow quasi-particle states, in qualitative agreement with lattice QCD studies [44]. Realistic values of $\Upsilon(1S, 2S)$ masses in fact allow the formation temperature T_{form} of $\Upsilon(1S)$ nearby T_c in line with the claim of [18,19] that hadrons form themselves at temperatures $T_c \approx T_{fo} \approx 155$ MeV. Insofar, the mystery "why $T_{fo} \approx T_c$?" could be resolved by a dynamical process within such a scenario: hadronization is the transit of a broad-to-narrow spectral functions within a few-MeV temperature intervals at T_c.

While quite promising, the proposed scenario was hampered by at least three issues. First, the finding of $T_{form} \approx T_c$ looks somewhat accidental and is not explicitly locked to a certain microscopic process; in addition, there is a slight tension due to the tendency of $T_{form} < T_c$ when deploying the exact PDG value of the $\Upsilon(2S)$ mass together with the $\Upsilon(1S)$ PDG value. Second, the formation of the $\Upsilon(2S)$ quasi-particle occurs at $T_{form}^{\Upsilon(2S)} < T_c$ due to the sequential formation, which, however, could be an artifact of the two-parameter model of U_0. Third, the envisaged scenario quantitatively fails for J/ψ since $T_{form}^{J/\psi} < T_c$ for the two-parameter model. It happens, however, that an improved three-parameter model U_0 overcomes such problems to some extent, i.e., charmonium formation at T_c is accomplished. An ideal choice of U_0 should deliver the quarkonia mass spectra (and other

properties as well) and quarkonia formation as the rapid shrinking of the spectral functions in a narrow temperature interval at T_c, including the excited states.

Formally, the hadronization of heavy-flavor probe quarkonia is determined by the potential U_0, which governs the crucial function G_m, thus partially decoupling it from the holographic background.

The herein proposed bottom-up scenario of quarkonia formation solely accommodates the properties of vector $c\bar{c}$ and $b\bar{b}$ states in the holographic bulk vector field $\mathcal{A}$. This is in contrast to microscopic studies, e.g., in [3,5,63–65], where the heavy-quark interaction with constituents of the ambient medium was dealt with in detail. Primordial contributions, early off-equilibrium yields as well as the corresponding feedings were also not accounted for. An important (yet) missing issue of the proposed scenario is a direct relation to observables in relativistic heavy-ion collisions. All this calls for further investigations.

Appendix A. Specific Features of the Holographic Gravity–Dilaton Background Adjusted to QCD Thermodynamics

The QCD$_{2+1}$(phys) equation of state obeys certain features. Among them are the minimum of the sound velocity at $T \approx 145$ MeV, $v_s^2(145 \text{ MeV}) \approx 0.15$, and the maximum of the interaction measure at $T \approx 200$ MeV, $(e-3p)/T^4|_{200 \text{ MeV}} \approx 4$ [21,22]. The contributions of charm and bottom quarks are negligible at $T \lesssim 200$ MeV [52]. The quoted temperature values bracket the pseudo-critical temperature $T_c = (156 \pm 1.5)$ MeV which is determined by a peak of the chiral susceptibility [20]. We focus here on the local minimum of the sound velocity and its mapping onto the gravity–dilaton background.

Deforming the AdS metric by putting a black hole with horizon at z_H yields the metric for the infinitesimal line elements squared (3) where $f(z, z_H)|_{z=z_H} = 0$ is a simple zero. In identifying the Hawking temperature $T(z_H) = -\partial_z f(z, z_H)|_{z=z_H}/4\pi$ with the temperature of the system at bulk boundary $z \to 0$ and the attributed Bekenstein–Hawking entropy density $s(z_H) = \frac{2\pi}{\kappa} \exp\{\frac{3}{2}A(z, z_H)|_{z=z_H}\}$, one holographically describes the thermodynamics. $f = 1$ at $T = 0$ refers to the vacuum.

The gravity–dilaton background is determined by the action in the Einstein frame:

$$S = \frac{1}{2\kappa} \int d^4x \, dz \sqrt{g_5} \left[R - \frac{1}{2}(\partial_z \phi)^2 - V(\phi) \right], \tag{A1}$$

where R stands for the curvature invariant and $\kappa = 8\pi G_5$. (For our purposes, the numerical values of κ and G_5 as well as k_V in (1) are irrelevant.) The field equations and equation of

motion for the metric coefficients and the dilaton follow from (A1) as

$$A'' = \frac{1}{2}A'^2 - \frac{1}{3}\phi'^2, \tag{A2}$$

$$f'' = -\frac{3}{2}A'f', \tag{A3}$$

$$\phi'' = -\left(\frac{2}{3}A' + \frac{f'}{f}\right)\phi' + \frac{1}{f}e^A\partial_\phi V \tag{A4}$$

to be solved with boundary conditions $A(z \to 0) \to -2\log(z/L)$, $\phi(0) = 0$, $\phi'(0) = 0$, $f(0) = 1$, $f(z_H) = 0$; the prime means differentiation with respect to z. The dilaton potential $V(\phi)$ is the central quantity [48]. If imposing certain conditions, one can describe the QCD-relevant cross-over (instead of the phase transitions of first or second order or a Hawking–Page transition). A necessary condition for a cross-over is (i) $\partial_\phi V/V$, as a function of ϕ, which has a local maximum and (ii) $\partial_\phi V/V < \sqrt{2/3}$ (for refinements, cf., [48]). Note that the adjustment of V to given lattice data is a non-local problem because there does not exist a point-to-point relation between $V(\phi)$ and relevant thermodynamic quantities (e.g., sound velocity as a function of the temperature).

The three-parameter ansatz:

$$-L^2 V = 12\cosh(\gamma\phi) + \phi_2\phi^2 + \phi_4\phi^4 \tag{A5}$$

is sufficient for a satisfactory description of the lattice QCD_{2+1}(phys) data [21,22] (more parameters are required for a perfect match of the various thermodynamic state variables as a function of the temperature within the full data range) by coefficients $(\gamma, \phi_2, \phi_4) = (0.568, -1.92, -0.04)$ together with $L^{-1} = 1.99$ GeV, see Figure 5-left in [59]. In fact, the aforementioned conditions are met: a maximum of $\partial_\phi V/V = 0.58$ at $\phi = 1.84$.

In general, the sound velocity squared, $v_s^2 = \frac{d\log T}{d\log s}$ acquires a local minimum if $s(T)$, or $s(T)/T^4$ has an inflection point. Surprisingly, neither $T(z_H)$ nor $s(z_H)$ display such a feature. Instead, both $T(z_H)$ and $s(z_H)$ are monotonous functions of z_H, as can be seen in Figure A1. This means, the minimum of the sound velocity is caused by a subtle interplay of derivatives of $T(z_H)$ and $s(z_H)$. Displaying the sound velocity squared by $v_s^2(z_H) = \partial_{z_H}\log T/\partial_{z_H}\log s$, the local minimum is determined by

$$\partial_{z_H}^2 T/\partial_{z_H}T - \partial_{z_H}T/T - \partial_{z_H}^2 A(z = z_H)/\partial_{z_H}A(z = z_H) = 0. \tag{A6}$$

These individual terms are exhibited in Figure A2. It turns out that the actually chosen parameters facilitate the minimum of sound velocity at the crossing of the fat solid and thin solid curves at $z_H/L = 5.17$, corresponding to $T = 152$ MeV, i.e., nearby T_c and thus T_{fo}.

In contrast to $T(z_H)$ and $A(z, z_H)|_{z=z_H}$, the dilaton profile $\phi(z, z_H)$ has a marked imprint of the QCD specifics: this exhibits inflection points in both the z direction and z_H direction, as can be seen in Figure A3. This is a remarkable property which makes the use of the QCD-related gravity–dilaton background distinct in comparison with the schematic ansätze, which additionally misses the consistent interrelations of the quantities A, f and ϕ via field equations. Note that the dilaton explicitly enters the quarkonium action (1), thus directly leaving its imprints related to quarkonium formation.
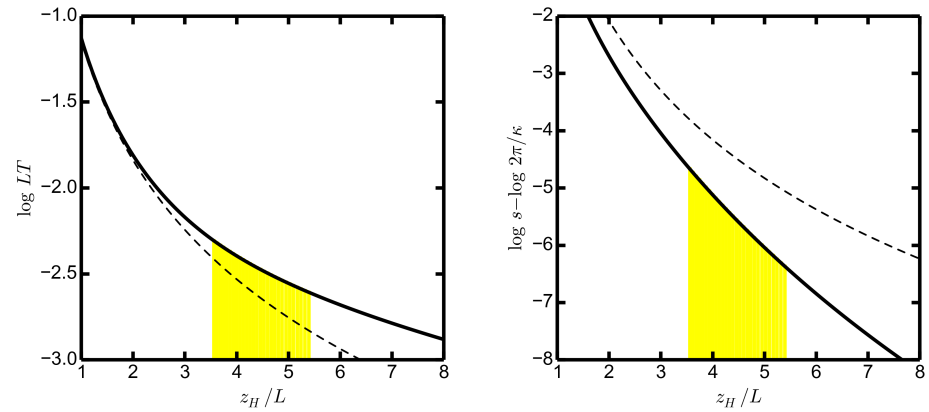
Figure A1. The logarithms of temperature, $\log LT$ (**left panel**), and entropy density, $\log s - \log 2\pi/\kappa = \frac{3}{2}A(z_H, z_H)$ (**right panel**), as a function of z_H/L. Dashed curves are for $LT = 1/(\pi z_H)$ (**left**) and $\frac{3}{2}A = -3\log z_H/L$ (**right**). The colored regions are for $z_H = [z_H^{v_s^2}, z_H^{\hat{I}}]$, which are determined by $T_c^{v_s^2} = 145$ MeV (position of the minimum sound velocity) and $T_c^{\hat{I}} = 200$ MeV (position of the maximum of interaction measure $\hat{I} = (e - 3p)/T^4$) according to [22].
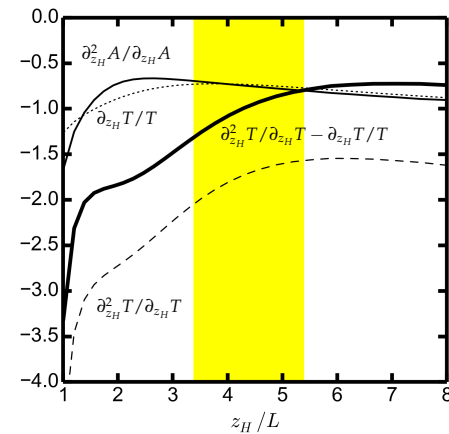

Figure A2. The terms entering (A6) multiplied by z_H: $\partial_{z_H}^2 T/\partial_{z_H} T$—dashed curve; $\partial_{z_H} T/T$—dotted curve; $\partial_{z_H}^2 T/\partial_{z_H} T - \partial_{z_H} T/T$—fat solid curve; and $\partial_{z_H}^2 A/\partial_{z_H} A$—thin solid curve. The yellow region is as in Figure A1.
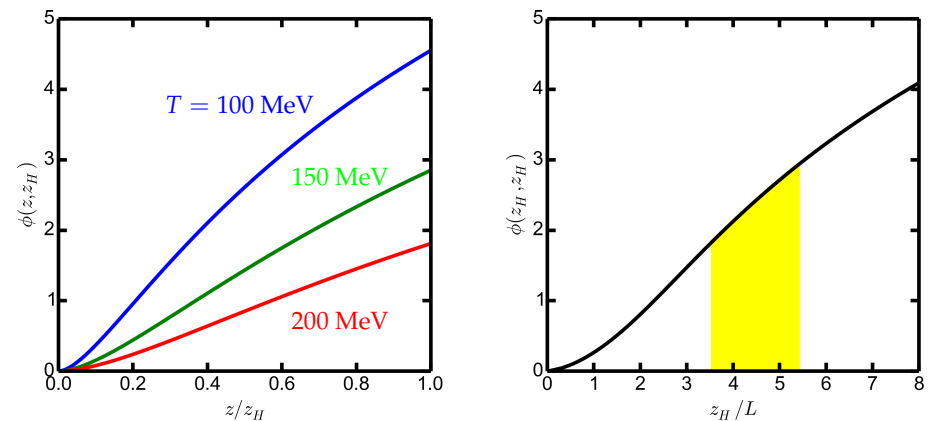

Figure A3. The dilaton profile $\phi(z, z_H)$ as a function of z/z_H (**left panel**, for $z_H/L = 9.28$, 5.22 and 3.52 corresponding to $T = 100$ (blue), 150 (green), 200 (red) MeV with inflection points at $z/z_H = 0.20$, 0.33, 0.44) and $\phi(z, z_H)|_{z=z_H}$ as a function of z_H (**right panel**, the inflection point is at $z_H/L = 2.91$).

References

1. Antinori, F.; Dainese, A.; Giubellino, P.; Greco, V.; Lombardo, M.P.; Scomparin, E. (Eds.) Proceedings of the 27th International Conference on Ultrarelativistic Nucleus-Nucleus Collisions (Quark Matter 2018), Venice, Italy, 14–19 May 2018. Available online: https://indico.cern.ch/event/656452/registrations/participants (accessed on 5 April 2021).
2. Antinori, F.; Dainese, A.; Giubellino, P.; Greco, V.; Lombardo, M.P.; Scomparin, E. (Eds.) Proceedings of the 28th International Conference on Ultrarelativistic Nucleus-Nucleus Collisions (Quark Matter 2019), Wuhan, China, 4–9 November 2019. Available online: https://indico.cern.ch/event/792436/page/19061-proceedings (accessed on 5 April 2021).
3. Strickland, M. Using bottomonium production as a tomographic probe of the quark-gluon plasma. In Proceedings of the 13th International Workshop in High pT Physics in the RHIC and LHC Era, Knoxville, TN, USA, 19–22 March 2019.
4. Prino, F.; Rapp, R. Open Heavy Flavor in QCD Matter and in Nuclear Collisions. *J. Phys. G* **2016**, *43*, 093002. [CrossRef]
5. Yao, X.; Müller, B. Quarkonium inside the quark-gluon plasma: Diffusion, dissociation, recombination, and energy loss. *Phys. Rev. D* **2019**, *100*, 014008. [CrossRef]
6. Rapp, R.; Gossiaux, P.B.; Andronic, A.; Averbeck, R.; Masciocchi, S.; Beraudo, A.; Bratkovskaya, E.; Braun-Munzinger, P.; Cao, S.; Dainese, A.; et al. Extraction of Heavy-Flavor Transport Coefficients in QCD Matter. *Nucl. Phys. A* **2018**, *979*, 21–86. [CrossRef]
7. Xu, Y.; Bass, S.A.; Moreau, P.; Song, T.; Nahrgang, M.; Bratkovskaya, E.; Gossiaux, P.; Aichelin, J.; Cao, S.; Greco, V.; et al. Resolving discrepancies in the estimation of heavy quark transport coefficients in relativistic heavy-ion collisions. *Phys. Rev. C* **2019**, *99*, 014902. [CrossRef]
8. Cao, S.; Coci, G.; Das, S.K.; Ke, W.; Liu, S.Y.F.; Plumari, S.; Song, T.; Xu, Y.; Aichelin, J.; Bass, S.; et al. Toward the determination of heavy-quark transport coefficients in quark-gluon plasma. *Phys. Rev. C* **2019**, *99*, 054907. [CrossRef]
9. Brambilla, N.; Escobedo, M.A.; Vairo, A.; Griend, P.V. Transport coefficients from in medium quarkonium dynamics. *Phys. Rev. D* **2019**, *100*, 054025. [CrossRef]
10. Song, T.; Moreau, P.; Aichelin, J.; Bratkovskaya, E. Exploring non-equilibrium quark-gluon plasma effects on charm transport coefficients. *Phys. Rev. C* **2020**, *101*, 044901. [CrossRef]
11. Chattopadhyay, C.; Heinz, U.W. Hydrodynamics from free-streaming to thermalization and back again. *Phys. Lett. B* **2020**, *801*, 135158. [CrossRef]
12. Bazow, D.; Heinz, U.W.; Strickland, M. Second-order (2+1)-dimensional anisotropic hydrodynamics. *Phys. Rev. C* **2014**, *90*, 054910. [CrossRef]
13. Katz, R.; Gossiaux, P.B. The Schrödinger–Langevin equation with and without thermal fluctuations. *Ann. Phys.* **2016**, *368*, 267. [CrossRef]
14. Blaizot, J.P.; Escobedo, M.A. Quantum and classical dynamics of heavy quarks in a quark-gluon plasma. *J. High Energy Phys.* **2018**, *2018*, 34. [CrossRef]
15. Blaizot, J.P.; Escobedo, M.A. Approach to equilibrium of a quarkonium in a quark-gluon plasma. *Phys. Rev. D* **2018**, *98*, 074007. [CrossRef]
16. Brambilla, N.; Escobedo, M.A.; Soto, J.; Vairo, A. Heavy quarkonium suppression in a fireball. *Phys. Rev. D* **2018**, *97*, 074009. [CrossRef]
17. Rothkopf, A. Heavy Quarkonium in Extreme Conditions. *Phys. Rept.* **2020**, *858*, 1–117. [CrossRef]
18. Braun-Munzinger, P.; Dönigus, B. Loosely-bound objects produced in nuclear collisions at the LHC. *Nucl. Phys. A* **2019**, *987*, 144–201. [CrossRef]
19. Andronic, A.; Braun-Munzinger, P.; Redlich, K.; Stachel, J. Decoding the phase structure of QCD via particle production at high energy. *Nature* **2018**, *561*, 321–330. [CrossRef]
20. Bazavov, A.; Ding, H.-T.; Hegde, P.; Kaczmarek, O.; Karsch, F.; Karthik, N.; Laermann, E.; Lahiri, A.; Larsen, R.; Li, S.-T.; et al. Chiral crossover in QCD at zero and non-zero chemical potentials. *Phys. Lett. B* **2019**, *795*, 15–21. [CrossRef]
21. Borsanyi, S.; Fodor, Z.; Hoelbling, C.; Katz, S.D.; Krieg, S.; Szabo, K.K. Full result for the QCD equation of state with 2+1 flavors. *Phys. Lett. B* **2014**, *730*, 99–104. [CrossRef]
22. Bazavov, A.; Bhattacharya, T.; DeTar, C.; Ding, H.-T.; Gottlieb, S.; Gupta, R.; Hegde, P.; Heller, U.M.; Karsch, F.; Laermann, E.; et al. Equation of state in (2+1)-flavor QCD. *Phys. Rev. D* **2014**, *90*, 094503. [CrossRef]
23. Suganuma, H.; Doi, T.M.; Redlich, K.; Sasaki, C. Relating Quark Confinement and Chiral Symmetry Breaking in QCD. *J. Phys. G* **2017**, *44*, 124001. [CrossRef]
24. Bellwied, R.; Noronha-Hostler, J.; Parotto, P.; Vazquez, I.P.; Ratti, C.; Stafford, J.M. Freeze-out temperature from net-kaon fluctuations at energies available at the BNL Relativistic Heavy Ion Collider. *Phys. Rev. C* **2019**, *99*, 034912. [CrossRef]
25. Colangelo, P.; Giannuzzi, F.; Nicotri, S. In-medium hadronic spectral functions through the soft-wall holographic model of QCD. *J. High Energy Phys.* **2012**, *2012*, 76. [CrossRef]
26. Colangelo, P.; Giannuzzi, F.; Nicotri, S. Holographic Approach to Finite Temperature QCD: The Case of Scalar Glueballs and Scalar Mesons. *Phys. Rev. D* **2009**, *80*, 094019. [CrossRef]
27. Colangelo, P.; Fazio, F.D.; Giannuzzi, F.; Jugeau, F.; Nicotri, S. Light scalar mesons in the soft-wall model of AdS/QCD. *Phys. Rev. D* **2008**, *78*, 055009. [CrossRef]
28. Zöllner, R.; Kämpfer, B. Holographically emulating sequential versus instantaneous disappearance of vector mesons in a hot environment. *Phys. Rev. C* **2016**, *94*, 045205. [CrossRef]
29. Zöllner, R.; Kämpfer, B. Holography at QCD-T_c. *J. Phys. Conf. Ser.* **2017**, *878*, 012023. [CrossRef]

30. Zöllner, R.; Kämpfer, B. Holographic vector mesons in a dilaton background. *J. Phys. Conf. Ser.* **2018**, *1024*, 012003. [CrossRef]
31. Braga, N.R.F.; Contreras, M.A.M.; Diles, S. Holographic model for heavy-vector-meson masses. *EPL Europhys. Lett.* **2016**, *115*, 31002. [CrossRef]
32. Braga, N.R.F.; Contreras, M.A.M.; Diles, S. Holographic Picture of Heavy Vector Meson Melting. *Eur. Phys. J. C* **2016**, *76*, 598. [CrossRef]
33. Fujita, M.; Fukushima, K.; Misumi, T.; Murata, M. Finite-temperature spectral function of the vector mesons in an AdS/QCD model. *Phys. Rev. D* **2009**, *80*, 035001. [CrossRef]
34. Fujita, M.; Kikuchi, T.; Fukushima, K.; Misumi, T.; Murata, M. Melting Spectral Functions of the Scalar and Vector Mesons in a Holographic QCD Model. *Phys. Rev. D* **2010**, *81*, 065024. [CrossRef]
35. Grigoryan, H.R.; Hohler, P.M.; Stephanov, M.A. Towards the Gravity Dual of Quarkonium in the Strongly Coupled QCD Plasma. *Phys. Rev. D* **2010**, *82*, 026005. [CrossRef]
36. Braga, N.R.F.; Ferreira, L.F.; Vega, A. Holographic model for charmonium dissociation. *Phys. Lett. B* **2017**, *774*, 476–481. [CrossRef]
37. Andreev, O. Aspects of quarkonium propagation in a thermal medium as seen by string models. *Phys. Rev. D* **2019**, *100*, 026013. [CrossRef]
38. Vega, A.; Contreras, M.A.M. Melting of scalar hadrons in an AdS/QCD model modified by a thermal dilaton. *Nucl. Phys. B* **2019**, *942*, 410–418. [CrossRef]
39. Mamani, L.A.H.; Miranda, A.S.; Zanchin, V.T. Melting of scalar mesons and black-hole quasinormal modes in a holographic QCD model. *Eur. Phys. J. C* **2019**, *79*, 435. [CrossRef]
40. Dudal, D.; Mertens, T.G. Melting of charmonium in a magnetic field from an effective AdS/QCD model. *Phys. Rev. D* **2015**, *91*, 086002. [CrossRef]
41. Bazavov, A.; Karsch, F.; Maezawa, Y.; Mukherjee, S.; Petreczky, P. In-medium modifications of open and hidden strange-charm mesons from spatial correlation functions. *Phys. Rev. D* **2015**, *91*, 054503. [CrossRef]
42. Kim, S.; Petreczky, P.; Rothkopf, A. Quarkonium in-medium properties from realistic lattice NRQCD. *J. High Energy Phys.* **2018**, *2018*, 088. [CrossRef]
43. Kruse, A.L.; Ding, H.T.; Kaczmarek, O.; Ohno, H.; Sandmeyer, H. Insight into Thermal Modifications of Quarkonia From a Comparison of Continuum-Extrapolated Lattice Results to Perturbative QCD. *Proceedings* **2019**, *10*, 45. [CrossRef]
44. Larsen, R.; Meinel, S.; Mukherjee, S.; Petreczky, P. Excited bottomonia in quark-gluon plasma from lattice QCD. *Phys. Lett. B* **2020**, *800*, 135119. [CrossRef]
45. Gubser, S.S.; Nellore, A. Mimicking the QCD equation of state with a dual black hole. *Phys. Rev. D* **2008**, *78*, 086007. [CrossRef]
46. Finazzo, S.I.; Rougemont, R.; Marrochio, H.; Noronha, J. Hydrodynamic transport coefficients for the non-conformal quark-gluon plasma from holography. *J. High Energy Phys.* **2015**, *2015*, 51. [CrossRef]
47. Finazzo, S.I.; Noronha, J. A holographic calculation of the electric conductivity of the strongly coupled quark-gluon plasma near the deconfinement transition. *Phys. Rev. D* **2014**, *89*, 106008. [CrossRef]
48. Zöllner, R.; Kämpfer, B. Phase structures emerging from holography with Einstein gravity—Dilaton models at finite temperature. *Eur. Phys. J. Plus* **2020**, *135*, 304. [CrossRef]
49. Bartz, S.P.; Dhumuntarao, A.; Kapusta, J.I. Dynamical AdS/Yang-Mills model. *Phys. Rev. D* **2018**, *98*, 026019. [CrossRef]
50. Jarvinen, M.; Kiritsis, E. Holographic Models for QCD in the Veneziano Limit. *J. High Energy Phys.* **2012**, *2012*, 2. [CrossRef]
51. Gursoy, U.; Kiritsis, E.; Mazzanti, L.; Michalogiorgakis, G.; Nitti, F. Improved Holographic QCD. In *From Gravity to Thermal Gauge Theories: The AdS/CFT Correspondence*; Lecture Notes in Physics; Springer: Berlin/Heidelberg, Germany, 2011; Volume 828, pp. 79–146.
52. Borsanyi, S.; Fodor, Z.; Guenther, J.; Kampert, K.-H.; Katz, S.D.; Kawanai, T.; Kovacs, T.G.; Mages, S.W.; Pasztor, A.; Pittler, F.; et al. Calculation of the axion mass based on high-temperature lattice quantum chromodynamics. *Nature* **2016**, *539*, 69–71. [CrossRef]
53. Karch, A.; Katz, E.; Son, D.T.; Stephanov, M.A. Linear confinement and AdS/QCD. *Phys. Rev. D* **2006**, *74*, 015005. [CrossRef]
54. Afonin, S.S. Generalized Soft Wall model. *Phys. Lett. B* **2013**, *719*, 399–403. [CrossRef]
55. Chumbes, A.E.R.; da Silva, J.M.H.; Hott, M.B. A model to localize gauge and tensor fields on thick branes. *Phys. Rev. D* **2012**, *85*, 085003. [CrossRef]
56. Eto, M.; Kawaguchi, M. Localization of gauge bosons and the Higgs mechanism on topological solitons in higher dimensions. *J. High Energy Phys.* **2019**, *2019*, 98. [CrossRef]
57. Arai, M.; Blaschke, F.; Eto, M.; Sakai, N. Grand Unified Brane World Scenario. *Phys. Rev. D* **2017**, *96*, 115033. [CrossRef]
58. Braga, N.R.F.; Ferreira, L.F. Heavy meson dissociation in a plasma with magnetic fields. *Phys. Lett. B* **2018**, *783*, 186–192. [CrossRef]
59. Zöllner, R.; Kampfer, B. Holographic vector meson melting in a thermal gravity-dilaton background related to QCD. *Eur. Phys. J. Spec. Top.* **2020**, *229*, 3585–3594. [CrossRef]
60. Hohler, P.M.; Yin, Y. Charmonium moving through a strongly coupled QCD plasma: A holographic perspective. *Phys. Rev. D* **2013**, *88*, 086001. [CrossRef]
61. Teaney, D. Finite temperature spectral densities of momentum and R-charge correlators in $N = 4$ Yang Mills theory. *Phys. Rev. D* **2006**, *74*, 045025. [CrossRef]
62. Ebert, D.; Faustov, R.N.; Galkin, V.O. Spectroscopy and Regge trajectories of heavy quarkonia and B_c mesons. *Eur. Phys. J. C* **2011**, *71*, 1825. [CrossRef]

63. Hoelck, J.; Nendzig, F.; Wolschin, G. In-medium Y suppression and feed-down in UU and PbPb collisions. *Phys. Rev. C* **2017**, *95*, 024905. [CrossRef]

64. Du, X.; Liu, S.Y.F.; Rapp, R. Extraction of the Heavy-Quark Potential from Bottomonium Observables in Heavy-Ion Collisions. *Phys. Lett. B* **2019**, *796*, 20–25. [CrossRef]

65. Du, X.; Rapp, R.; He, M. Color Screening and Regeneration of Bottomonia in High-Energy Heavy-Ion Collisions. *Phys. Rev. C* **2017**, *96*, 054901. [CrossRef]